


FULL PAPER

Open Access



Temporary slip speed increases during short-term slow slip events with durations of one to three hours

Akio Katsumata^{1*} , Kazuki Miyaoka², Takahiro Tsuyuki³, Satoshi Itaba⁴, Masayuki Tanaka⁵, Takeo Ito⁶, Akiteru Takamori⁷ and Akito Araya⁸

Abstract

Temporary slip speed increases with durations of 1–3 h were identified during short-term slow slip events in records of borehole and laser strainmeters in the Tokai region, Japan. They were found by searching for peaks of correlation coefficients between stacked strain data and ramp functions with rise times of 1 and 2 h. Although many of the strain steps were considered due to noise, some strain steps occurred with simultaneous activation of the deep tectonic tremors and shared source areas with the tremors. From 2016 to 2022, we observed five strain steps with simultaneous activation of tectonic tremors and coincidence of source locations with the tremors. Those strain steps occurred during short-term slow slip events and were temporary slip speed increases of the slow slip events. Those strain steps seemed to be related to successive occurrences with source migration of short-term slow slip events. The detrended strain steps corresponded to plate boundary slip events of moment magnitude around 5, which was consistent with the scaling law of slow earthquakes.

Keywords Slow earthquake, Short-term slow slip event, Variation of slip speed during slow earthquakes, Borehole and laser strainmeters

*Correspondence:

Akio Katsumata

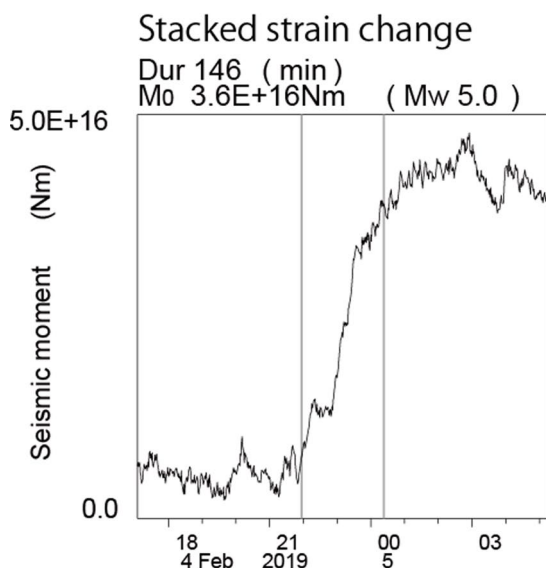
akatsuma@sus.u-toyama.ac.jp

Full list of author information is available at the end of the article

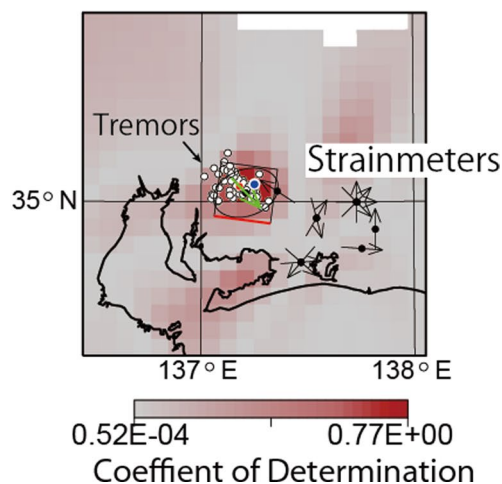


© The Author(s) 2024. **Open Access** This article is licensed under a Creative Commons Attribution 4.0 International License, which permits use, sharing, adaptation, distribution and reproduction in any medium or format, as long as you give appropriate credit to the original author(s) and the source, provide a link to the Creative Commons licence, and indicate if changes were made. The images or other third party material in this article are included in the article's Creative Commons licence, unless indicated otherwise in a credit line to the material. If material is not included in the article's Creative Commons licence and your intended use is not permitted by statutory regulation or exceeds the permitted use, you will need to obtain permission directly from the copyright holder. To view a copy of this licence, visit <http://creativecommons.org/licenses/by/4.0/>.

Graphical Abstract



Estimation of source location by coefficient of determination



Introduction

Various types of slow earthquakes occur along subduction zones in both the deep and shallow parts of the source areas of megathrust earthquakes. The source durations and seismic moments of slow earthquakes vary greatly. Tectonic tremors, including shallow tremors and low-frequency earthquakes (LFEs), have a characteristic period of 0.2–2 s (Obara 2002; Rogers and Dragert 2003; Katsumata and Kamaya 2003). Both deep and shallow very low frequency earthquakes (VLFs) have a dominant period of 10–50 s (Obara and Ito 2005; Ito et al. 2007; Ghosh et al. 2015). Bletery et al. (2017) detected migrations of LFEs at time scales between 30 min and 32 h, and interpreted them as secondary slip front propagation. Aiken and Obara (2021) analyzed LFE clusters and detected slowly slipping fault motion, whose durations ranged from 10^4 to 10^6 s. Along the Nankai Trough subduction zone in Southwest Japan, slow slip events (SSEs) of various source durations have been observed. The Tokai SSEs have source durations of a couple to several years (Ozawa et al. 2005; Kobayashi and Yoshida 2004; Ozawa et al. 2016). SSEs around the Bungo channel can last from several months to a couple of years (Hirose et al. 1999; Hirose and Obara 2005; Seshimo and Yoshioka 2022). In a wide area along the Nankai Trough subduction zone, SSEs of about several days' duration, called short-term slow slip events (S-SSEs), have been

observed (Obara et al. 2004; Kobayashi et al. 2006). SSEs with longer durations than S-SSEs are called long-term SSEs. SSEs often accompany tectonic tremors, and they are identified as episodic tremor and slip (ETS) (Rogers and Dragert 2003; Obara et al. 2004). VLFs are also related to the activities of ETSs (Ito et al. 2007). Fukao et al. (2021) reported an aseismic slip with a rise time around 1 h at the Izu-Bonin Trench, which was a different type of slow earthquake from that seen along the Nankai Trough subduction zone. The moment rate of the event found by Fukao et al. (2021) was much larger than that of the slow earthquakes along the Nankai Trough.

The durations of SSEs in Cascadia, North America, are 2–4 weeks (Miller et al. 2002). Whereas SSEs along the Hikurangi subduction zone, New Zealand, have durations ranging from 6 days to 1.5 years, with SSEs at shallower depths having shorter durations (Wallace and Beavan 2010). SSEs in southern Mexico with durations of several months have also been reported (Kostoglodov et al. 2003; Cruz-Atienza et al. 2021).

Because the sizes of slow earthquake sources are distributed over a wide range, a single instrument cannot cover the entire observation range of slow earthquakes. Tremors and VLFs are detected with seismometers. Observation data from S-SSEs are mainly obtained with highly sensitive strainmeters (Kobayashi et al. 2006) and tiltmeters (Hirose and Obara 2005).

S-SSEs are also detected with GNSS (Nishimura 2014; Okada et al. 2022). Crustal deformation due to long-term SSEs along the Nankai Trough subduction zone and most of SSEs in other regions are measured mainly by the GNSS network (e.g. Hirose et al. 1999; Dragert et al. 2001).

Ide et al. (2007) have pointed out the existence of a scaling law among slow earthquakes; seismic moment is approximately proportional to event duration. Ide and Beroza (2023) updated the event list related to the scaling law, and discussed the rupture propagation process of slow earthquakes. Slow earthquakes with source durations greater than several tens of seconds and less than a few days were reported based on strain rate changes observed by borehole strainmeters (Hawthorne and Rubin 2013), LFE migration analyses (Bletery et al. 2017; Aiken and Obara 2021), and ocean bottom pressure gauges (Fukao et al. 2021). Hawthorne and Rubin (2013) found correlated strain rate changes observed by borehole strainmeters with seismic amplitude changes with durations from 15 min to 16 h in central Cascadia. Bletery et al. (2017) estimated the seismic moment of the

slow earthquakes detected by LFE migration by summing up the seismic moment of LFEs. It is difficult to get a direct observation about the slip amount during such slow earthquakes.

There is a gap of direct observation of seismic moment in the duration range between several tens of seconds of VLFES and a few days of S-SSEs along the Nankai Trough. It is important to estimate the seismic moments of slow earthquakes with such durations to understand the features of the slow earthquake group related to ETS along the Nankai Trough. We aimed to detect slow earthquakes with durations between those of VLFES and S-SSEs and to estimate their seismic moments using strainmeter data. Since strainmeters record tidal responses, strain changes shorter than 6 h have a better signal–noise ratio. We searched for SSEs with durations of one to several hours in crustal deformation data measured by borehole and laser strainmeters in the Tokai region, Japan, where the Philippine Sea plate subducts beneath the Eurasia plate from the Nankai trough (Fig. 1). In Fig. 1, epicenters of the tectonic tremor (Imanishi et al. 2011) and source areas of S-SSEs (e.g.

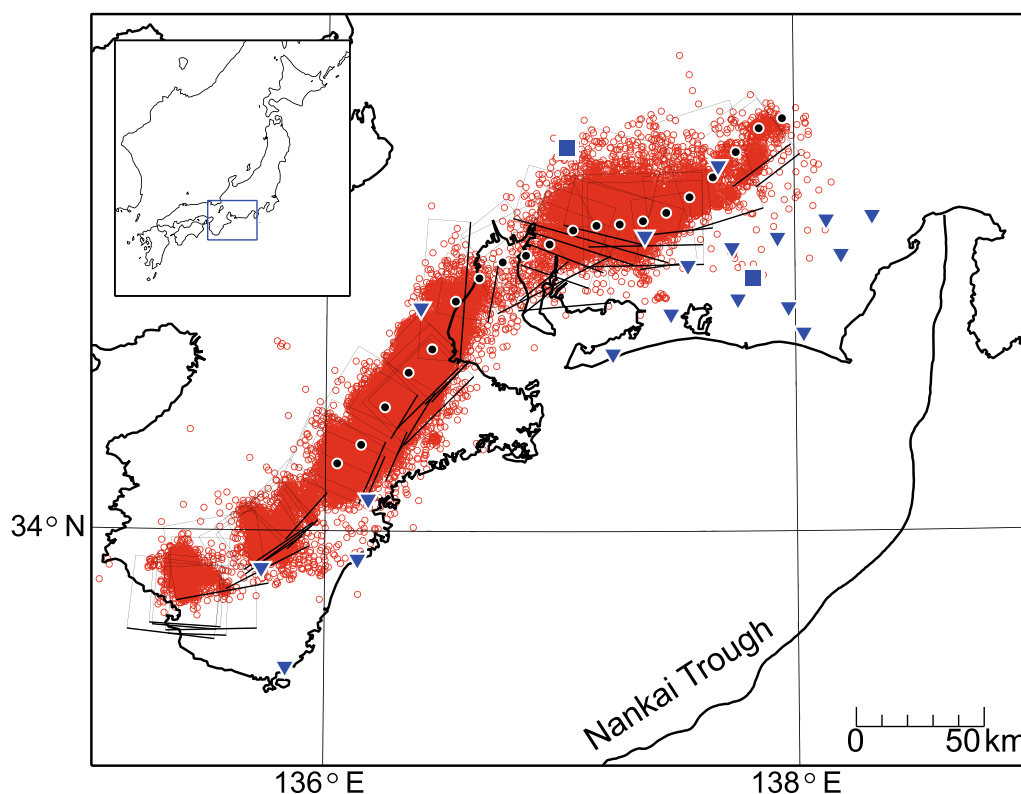


Fig. 1 Source Area of investigated slow slip events. The blue rectangle in the inset map of Japan shows the map area. Epicenters of the tectonic tremors from 2016 to 2022 estimated by the method of Imanishi et al. (2011) (red circles) and S-SSE source areas from 2021 to 2022 (e.g. Japan Meteorological Agency, 2021) (black rectangles) are shown. The period for S-SSEs was limited to two years to avoid too many plots. The blue triangles and rectangles show the borehole and laser strainmeter locations, respectively. The black dots show the assumed fault center locations used in the stacking method

Japan Meteorological Agency 2021) are shown. As a result, we identified some strain steps with durations of 1–3 h, which were temporary slip speed increases during S-SSEs. In this article, we describe our analysis of these strain steps.

Data

We analyzed strain data obtained using borehole (Ishii et al. 1997a, b) and laser strainmeters (Araya et al. 2002; Katsumata et al. 2010) installed at the stations listed in Table 1. Station locations are shown in Additional file 1: Fig. S1. We selected the Tokai region of the Nankai Trough subduction zone in Japan for our analysis because of the dense distribution of strainmeters there. Data of 1 sample/min were used, which were obtained by decimating the original data of higher sampling rates. Sampling rates of the original data were 1 sample/s or higher. Before the strain step analysis, the strain data were corrected for tidal and atmospheric pressure responses with the BAYTAP program (Tamura et al. 1991). Each strainmeter was equipped with a barometer at the site. Response correction matrices from Kamigaichi et al.

(1999) were applied to the data obtained with borehole strainmeters.

Detection of strain steps

At first, we searched for strain steps in the data of strainmeters. The procedure is described in this section. Then the source locations of the strain steps and their relationships with tectonic tremor activity are discussed in the latter sections.

We searched for strain steps with durations of around 1–4 h by calculating the correlation coefficient time series between stacked strain data and ramp functions (CC_{sr}). The strain data are contaminated with variation from various causes. To enhance the signal-to-noise ratio (S/N) and to exclude strain steps due to noise, we used the stacking method of Miyaoka and Yokota (2012) to analyze the strain data as follows:

- (1) Assume source parameters (fault center location, fault depth, strike, dip, rake, fault width, fault length, and seismic moment).
- (2) Calculate the theoretical strain value by the method of Okada (1992).
- (3) Change the polarity of the data when the theoretical value is negative.
- (4) Detrend the strain at each sensor using data before the investigated period.
- (5) Calculate the standard deviation of the data before the investigated period.
- (6) Reject data when the theoretical value is less than the standard deviation.
- (7) Normalize the strain change by the calculated standard deviation.
- (8) Sum the data from multiple channels.

In step (1), source locations were assumed as: longitudes from 136°E to 138°E with intervals of 0.1°; averaged latitude of S-SSEs estimated by Japan Meteorological Agency (e.g. Japan Meteorological Agency 2016) in each longitude interval; depths at the plate boundary (Hirose et al. 2008) beneath the assumed longitude and latitude. Because we expected that slow slip events of 1 h duration would have occurred in the source area of S-SSE such as tectonic tremors, VLFES, and S-SSEs sharing the same source area (Ito et al. 2007), the source locations were assumed based on those of S-SSEs. The assumed fault center locations are shown by black dots in Fig. 1. The strike and dip were set based on the plate configuration (Hirose et al. 2008), and the slip direction based on the plate motion parameters by Seno et al. (1993). The average fault length (31 km) and width (30 km) of estimated S-SSEs (e.g. Japan Meteorological Agency

Table 1 Stations from which strain data were obtained for this study

Station code	Latitude	Longitude	Type	Affiliation
ASAYA	34.937°N	137.542°E	Borehole	JMA
KURATA	34.975°N	138.197°E	Borehole	JMA
MIYAGUCH	34.818°N	137.755°E	Borehole	JMA
OCHIAI	35.111°N	138.332°E	Borehole	JMA
SAKUMA	34.999°N	137.731°E	Borehole	JMA
TAKATENJIN	34.699°N	138.035°E	Borehole	JMA
TAKAMATS	34.626°N	137.221°E	Borehole	JMA
TOMBE	34.789°N	137.971°E	Borehole	JMA
URUGI	35.288°N	137.674°E	Borehole	JMA
EFUJIKAW	35.097°N	138.135°E	Borehole	Shizuoka Pref.
HARUNO	35.034°N	137.926°E	Borehole	Shizuoka Pref.
HGM	33.867°N	135.732°E	Borehole	AIST
ICU	33.900°N	136.138°E	Borehole	AIST
KST	33.520°N	135.836°E	Borehole	AIST
MYM	34.112°N	136.182°E	Borehole	AIST
TSU	34.787°N	136.402°E	Borehole	AIST
TYE	34.766°N	137.469°E	Borehole	AIST
TYS	35.041°N	137.358°E	Borehole	AIST
FUNAGIRA	34.893°N	137.818°E	Laser	MRI and ERI
INUAYAMA	35.353°N	137.026°E	Laser	Nagoya Univ. and ERI

JMA Japan Meteorological Agency, AIST National Institute of Advanced Industrial Science and Technology, MRI Meteorological Research Institute, JMA, ERI Earthquake Research Institute, The University of Tokyo

2016) were used for the fault size. The seismic moment M_{0a} was set at $10^{1.5 \times 6.0 + 9.1}$ Nm for theoretical strains, which does not affect the estimation of the seismic moment of a strain step. This M_w is an approximate value of a background SSEs.

Strain data from January 2016 to December 2022 was surveyed with dividing the period into 10-day intervals. The leading part of 10 day length was added to each interval. In the stacking method, the detrending in step (4) and the standard deviation calculation in step (5) for the data of each sensor were based on the data in the leading part.

Rejection of data with prevailing noise over the signal in step (6) and normalization by standard deviation in step (7) were applied to reduce the contribution from noisy sensors in the stacked time series. The time series from the stacking method $A(t)$ is evaluated as follows:

$$A(t) = \frac{\sum_i \frac{o_i(t)p_i}{\sigma_i}}{\sum_i \frac{c_i p_i}{\sigma_i}}, \quad (1)$$

where t , $o_i(t)$, p_i , σ_i , and c_i denote time, observed strain change at the i th sensor, polarity of the theoretical strain (1 or -1), standard deviation of data, and the theoretical strain value. If $o_i(t)$ coincides with $c_i \frac{M_0(t)}{M_{0a}}$,

$$A(t) = \frac{M_0(t)}{M_{0a}}, \quad (2)$$

where $M_0(t)$ is the source time function of the slip event. Strain data at each sensor and stacked strain data for various assumed source locations are shown in Additional file 2: Fig. S2 and Additional file 3: S3 for an interval from 31 January, 2019.

CC_{sr} with ramp functions of 1, 2, and 4 h rise times were calculated. Because tidal components cannot be removed completely and the remaining tidal responses cause strain variation similar to a ramp function, we limited the rise time to less than 6 h. Time lengths before and after the ramp were set at double the rise time in the calculation of CC_{sr} , and trend was removed from both the stacked strain and the ramp function before the CC_{sr} calculation. An example of the analysis is shown in Fig. 2. The data shown in this figure include an S-SSE (M_w 5.9) from February 3, 2019 (Japan Meteorological Agency 2019).

The time series of CC_{sr} in Fig. 2b have many peaks. Figure 3 shows the ratios of positive peaks to the total number of peaks and troughs with a 0.005 interval of CC_{sr} . All the cases from 2016 to 2022 at the various fault locations are counted in the figure. The positive peaks indicate polarity consistent with the plate boundary slip event. The ratio of 0.5 corresponds to a random situation. When the number of positive peaks surpasses that of negative ones (troughs), the positive peaks would include strain steps due to the plate boundary slip events. For a rise time of 1 h, the ratio deviates to the higher side in the range of CC_{sr} greater than about 0.88 in Fig. 3. More than 300 peaks with $CC_{sr} > 0.88$ were found from 2016 to 2022, where duplicate counts due to different assumed source locations were removed. For a rise time of 4 h, higher side deviation was not observed. Positive peaks greater than 0.88 for an assumed rise time of 1 and 2 h were selected for the following analyses since they are consistent with the plate boundary slip events. When plural strain steps in overlapped time ranges were detected at different source locations or with different assumed rise times, the source location and the rise time of the highest correlation were adopted for further analysis. Though CC_{sr} peaks less than 0.88 could include those related to plate boundary slip events, identification of them is not easy due to contamination by various noises.

The ratio of positive peaks deviates from 0.5 in Fig. 3 for high CC_{sr} . The ratio was evaluated with a statistical test. If the time series of the CC_{sr} has random variation, the number of positive and negative peaks should be even. If the number of samples and the ratio of the positive peaks are assumed to be n and p , the expected number of positive peaks and dispersion are approximated as np and $np(1-p)$ for large np in a binomial distribution. Therefore, $Z = \frac{X-np}{\sqrt{np(1-p)}}$ would follow a normal distribution $N(0, 1)$, where X is a statistical variable. For a rejection region of 5%, $|Z|$ is greater than 1.96. Figure 4 shows the relationship between $\frac{X-np}{\sqrt{np(1-p)}}$ and CC_{sr} at peaks from 2016 to 2022, where X is the number of positive peaks and n the total number of peaks and troughs. For n and X , sums of data with CC_{sr} greater than the value on the horizontal axis were used. In most of the range in Fig. 4, Z is greater than 1.96, which means that

(See figure on next page.)

Fig. 2 (a) Example of stacked strain change. During this period, an S-SSE of M_w 5.9 (Japan Meteorological Agency 2019) was detected. The gray shade indicates the period shown in (c) and (d). (b) Time series of correlation coefficients between the stacked strain shown in (a) and a ramp function of 1 h rise time (CC_{sr}). The gray shade is the same as that in (a). (c) Detrended stacked strain shown in (a) during a 5-day interval that is the middle part of (a) and (b). (d) Detrended accumulated number of tectonic tremors in the same time period as that of (c). The periods shown in (c) and (d) with gray shades show durations of strain steps with $CC_{sr} > 0.88$

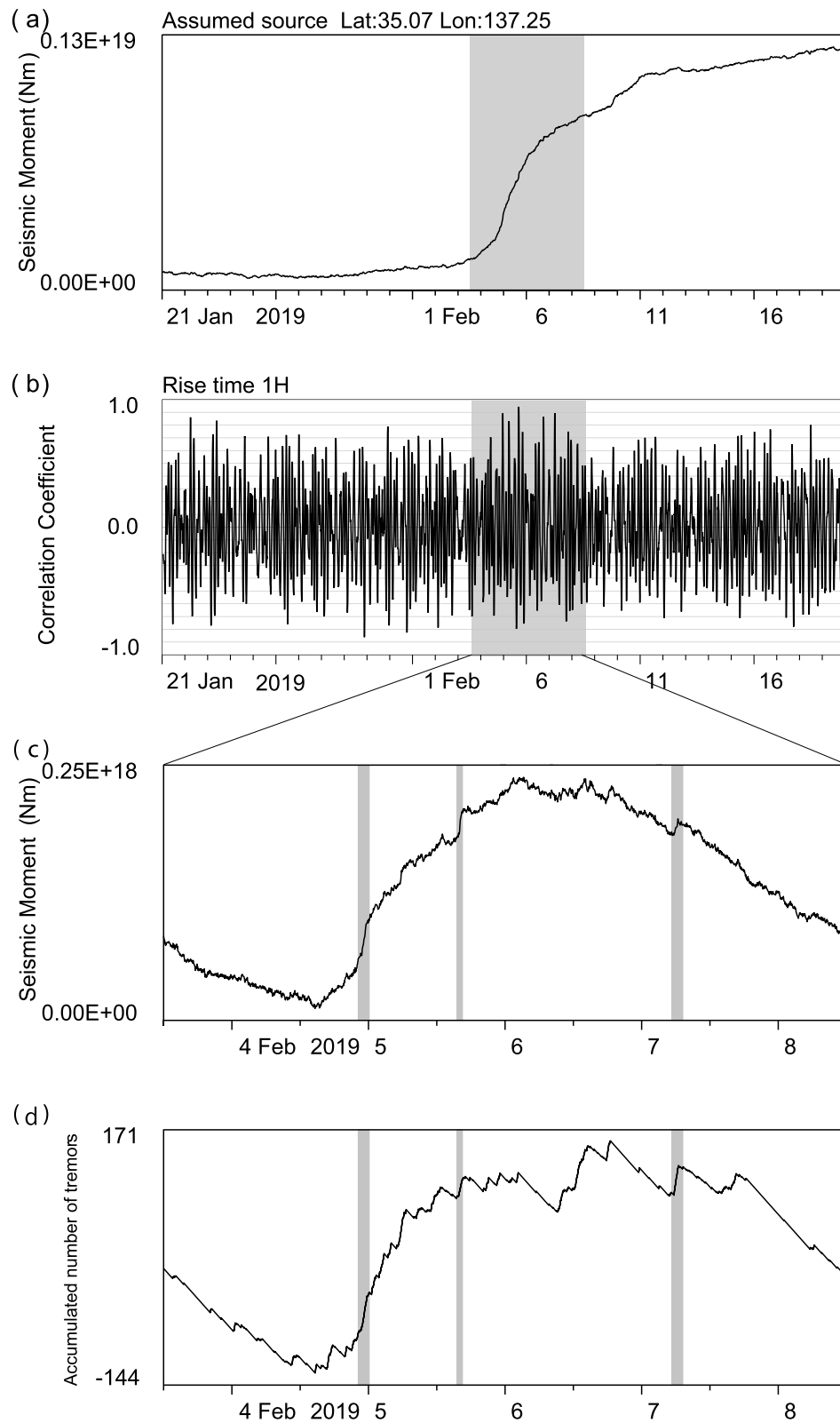


Fig. 2 (See legend on previous page.)

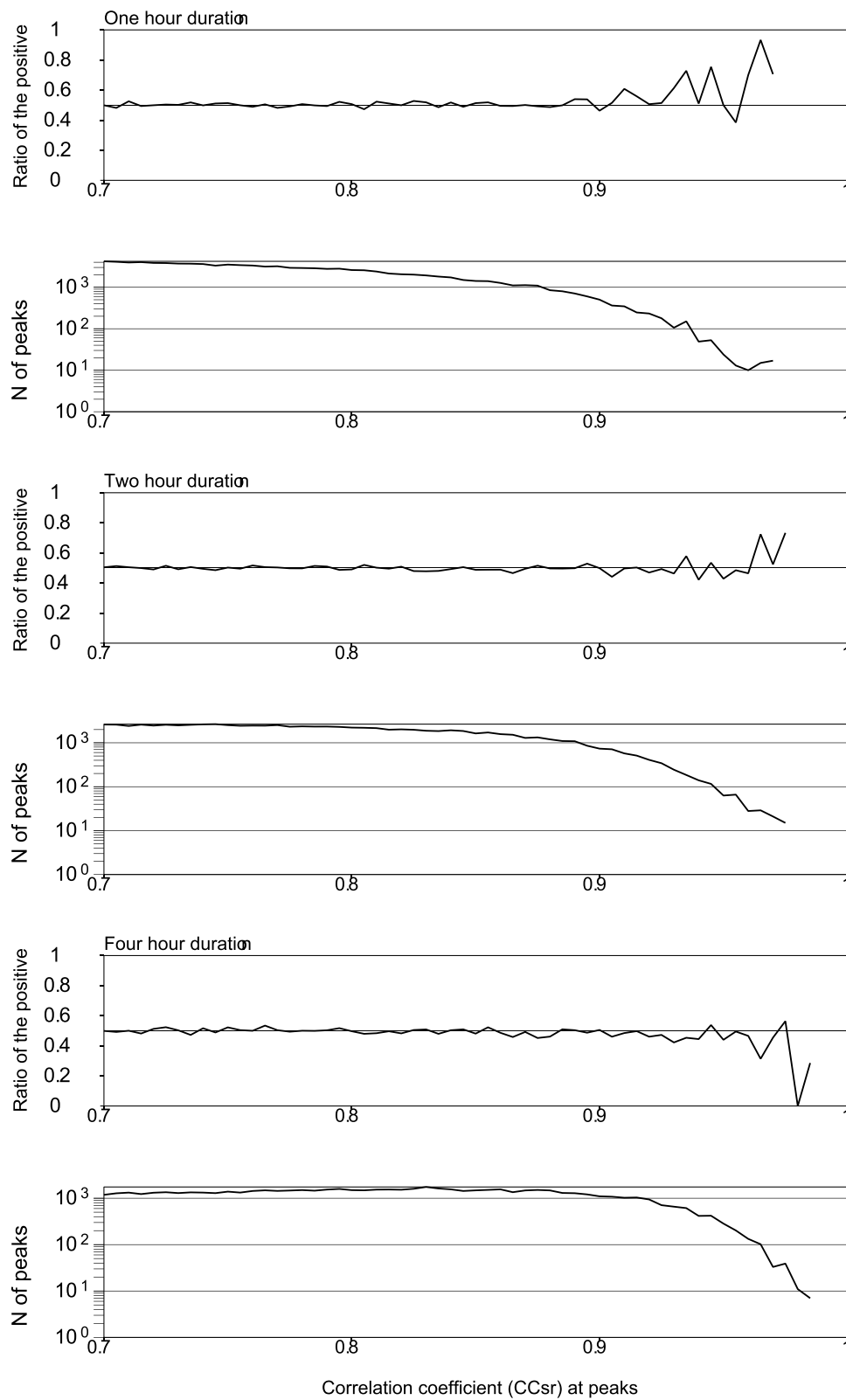


Fig. 3 Ratio of positive peaks (upper) to the total of peaks and troughs (lower) with CC_{sr} on the horizontal axes from 2016 to 2022. Three sets of graphs show those for assumed rise times of 1, 2, and 4 h of the ramp function

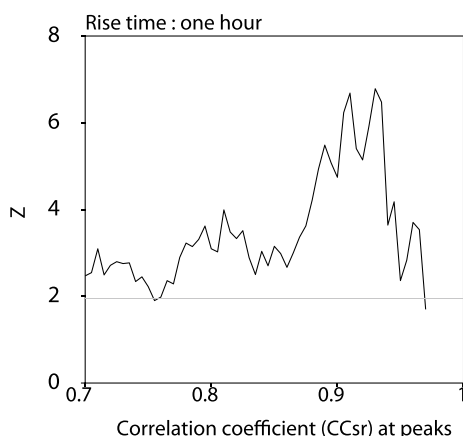


Fig. 4 Relationship between $Z = \frac{X-np}{\sqrt{np(1-p)}}$ and CC_{sr} at peaks (Fig. 2b), where X is number of positive peaks with CC_{sr} greater than that shown on the horizontal axis, n the total number of peaks and troughs with CC_{sr} greater than that shown on the horizontal axis, and p assumed ratio of positive peaks ($= 0.5$). The gray horizontal line denotes the threshold ($Z > 1.96$) for 5% rejection

the null hypothesis of $p = 0.5$ can be rejected. Especially, Z was large around $CC_{sr} = 0.93$.

Sources of strain steps

When a strain step with $CC_{sr} > 0.88$ was identified, its duration and location were estimated with data from selected sensors. In this section, sensor data with $|CC_{ir}| > 0.5$ were selected for duration and location estimations to reject noisy data, where CC_{ir} is a correlation coefficient between strain at an individual sensor and a ramp function with the rise time used to detect the strain step in the previous section. The value of 0.5 was used as a threshold of a clear correlation.

Stacked strain and its correlation coefficient with a ramp function (CC_{sr2}) were calculated to estimate the duration of the strain step from the data of $|CC_{ir}| > 0.5$. For CC_{sr2} , the same location and fault parameters used to detect the strain step in the previous section were assumed. Durations were estimated by identifying the peak value of the CC_{sr2} using the grid search method. In the grid search, the rise time of a ramp function was changed from 0.5 to 2 times rise time used for the strain step detection. Used data length was fixed at six times the rise time used in the detection, for which the leading and tail parts are of the same length of rise time assumed in the grid search when the rise time assumed in the grid search is double the rise time used for the detection. The rise time with the highest CC_{sr2} was adopted as the duration of the strain step. A graph of the duration grid search is shown in Additional file 4: Fig. S4.

The estimation error of the duration was evaluated using the statistical nature of the correlation coefficient. A correlation coefficient r approximately follows a normal distribution of $N(\frac{1}{2} \log \frac{1+r}{1-r}, \frac{1}{n-3})$, where n is the data number (e.g. Sugiyama et al. 2007). A range of duration where $\frac{1}{2} \log \frac{1+r}{1-r} > \frac{1}{2} \log \frac{1+r_p}{1-r_p} - \sqrt{\frac{1}{n-3}}$ is shown as an indication of uncertainty in Additional file 4: Fig. S4 and Table 2, where r_p is the peak value of CC_{sr2} . In Table 2, the shown value is half of the duration range.

Next, the source locations of the strain steps were investigated. Source locations were estimated by a method based on the coefficient of determination (r^2) between the observed and theoretical strain changes of individual sensors (Tsuyuki et al. 2017) as follows:

- (1) Set grid points (latitude and longitude) around the assumed source epicenter for the stacking method (Fig. 1). The grid point interval was assumed to be 7 km here.

Table 2 List of strain steps shown in Fig. 5

Mid time (JST) (Nm)	Latitude (deg)	Longitude (deg)	Depth (km)	Duration (min)	Seismic moment (M_w)	Strike, Dip, Rake	CC_{sr2}	CC_{st}
26 Nov. 2017 23:34	35.16	137.09	34.0	154 (+/- 33)	6.3E+16 (Mw5.1)	301, 14, 165	0.91	0.99
28 Nov. 2017 00:52	35.10	137.21	32.7	73 (+/- 20)	2.0E+16 (Mw4.8)	270, 17, 134	0.93	0.99
04 Feb. 2019 23:10	35.04	137.21	30.3	146 (+/- 25)	3.6E+16 (Mw5.0)	277, 16, 141	0.94	0.99
05 Feb. 2019 16:03	35.10	137.13	32.7	50 (+/- 21)	4.3E+16 (Mw5.0)	276, 16, 140	0.94	0.99
20 Jan. 2022 07:25	35.10	137.09	32.4	199 (+/- 17)	4.1E+16 (Mw5.0)	286, 15, 150	0.95	0.93

- (2) Set source depth, strike, and dip of the fault based on plate configuration (Hirose et al. 2008). The grid point was not set for a point with the plate boundary deeper than 60 km.
- (3) Set slip direction based on the plate motion (Seno et al. 1993).
- (4) Assume fault length and width. Both were set at 7 km as a small enough size to express a localized source.
- (5) Assume seismic moment. It was set at the same value as that obtained from strain step analysis.
- (6) Calculate the theoretical strains of individual sensors by the method of Okada (1992).
- (7) Calculate regression line between the calculated and the observed strains.
- (8) Calculate a coefficient of determination r^2 from the regression line. The intercept of the regression line is assumed to be zero, then r^2 is calculated as

$$r^2 = \frac{\sum_i \hat{y}_i^2}{\sum_i y_i^2}, \quad (3)$$

where i is an index for a sensor, y_i the observed strain step, and \hat{y}_i its regression.

- (9) Make a map of r^2 distribution. Examples are shown in Additional file 4: Fig. S4. The point with high r^2 is considered the probable source location of the slip event.

Graphs related to these analyses are shown in Additional file 4: Fig. S4.

The peak r^2 of the strain step at 16:03 on 5 February 2019 was 0.83 (Additional file 4: Fig. S4c). Z-transformed correlation coefficient $Z = \frac{\frac{1}{2} \log \frac{1+r}{1-r}}{1/\sqrt{n-3}}$ approximately follows the normal distribution $N(0, 1)$ (e.g. Sugiyama et al. 2007), where n is the data number. When a null hypothesis is set as $r = 0$, r^2 of 0.83 corresponds to $Z = 7.1$ which is much higher than the threshold 1.95 of 5% rejection. For the strain step at 23:10 on 4 February 2019 (the peak $r^2 = 0.77$, Fig. S4b), Z was 4.3. This indicates that such high r^2 was rarely caused by random noise.

It is preferable to express the region of high r^2 with parameterized values to compare it with other distributions. In the following part, we compare the r^2 distribution with the tectonic tremor distribution. One of the ways to express a region is fitting a diagram such as a circle or rectangle to it. A two-dimensional Gaussian distribution was fitted to the r^2 distribution here. The Gaussian distribution $f(x, y)$ was expressed as

where (x, y) denotes a horizontal coordinate and x_c, y_c, a_{11}, a_{12} , and a_{22} parameters of the Gaussian distribution. The parameters x_c, y_c, a_{11}, a_{12} , and a_{22} were determined with a grid search method by minimizing $\sum_i (r^2/r_{max}^2 - f(x_i, y_i))^2$, where (x_i, y_i) is a grid point of r^2 . The fitted distribution is shown with an ellipsoid ($a_{11}(x - x_c)^2 + 2a_{12}(x - x_c)(y - y_c) + a_{22}(y - y_c)^2 = 1$) in Figs. 5 and S4. CC_{sr} of six strain steps exceeded 0.88 in a 10-day interval from 31 January, 2019. Three of the six strain steps (Additional file 4: Fig. S4b,c,e) have relatively concentrated r^2 distributions. Since random noise should not make a concentrated distribution of r^2 , a concentrated r^2 distribution would mean that the corresponding strain step would be related to a localized plate boundary slip event.

After the estimation of the source location, the stacking is done again to estimate seismic moment of the strain steps. For this stacking, the fault center was assumed to be the center of the fitted ellipsoid, and the fault length and width were set at the average of the short and long diameters of the ellipsoid. The strike and dip of the fault were based on the plate configuration by Hirose et al. (2008). The slip direction was based on the plate motion by Seno et al. (1993).

Correlation with tectonic tremor activity

It is difficult to exclude the possibility of environmental noise as the cause of the detected strain steps completely. To get supporting evidence of plate boundary slip events as the cause of the strain steps, an independent observation was referred to. The open circles on the maps of Fig. 5 and Additional file 4: Fig S4 denote epicenters of tectonic tremors estimated by the method of Imanishi et al. (2011). An example of the accumulated number of tectonic tremors is shown in Fig. 2d. The periods shown by gray shades in Fig. 2c,d correspond to those of strain steps with $CC_{sr} > 0.88$. Accumulated number of tectonic tremors during the strain steps is shown in Additional file 4: Fig. S4. The correlation coefficient between the stacked strain and the accumulated number of tectonic tremors (CC_{st}) was calculated. Tremors within 50 km of epicentral distance from the assumed source location used in “Detection of Strain Steps” section (a black dot in Fig. 1) were counted. We used the assumed source location rather than the peak location of r^2 because some of the peak locations were far from the tremor clusters. The distance of 50 km was used to include tectonic tremors a

$$f(x, y) = \exp \left[-\{a_{11}(x - x_c)^2 + 2a_{12}(x - x_c)(y - y_c) + a_{22}(y - y_c)^2\}/2 \right], \quad (4)$$

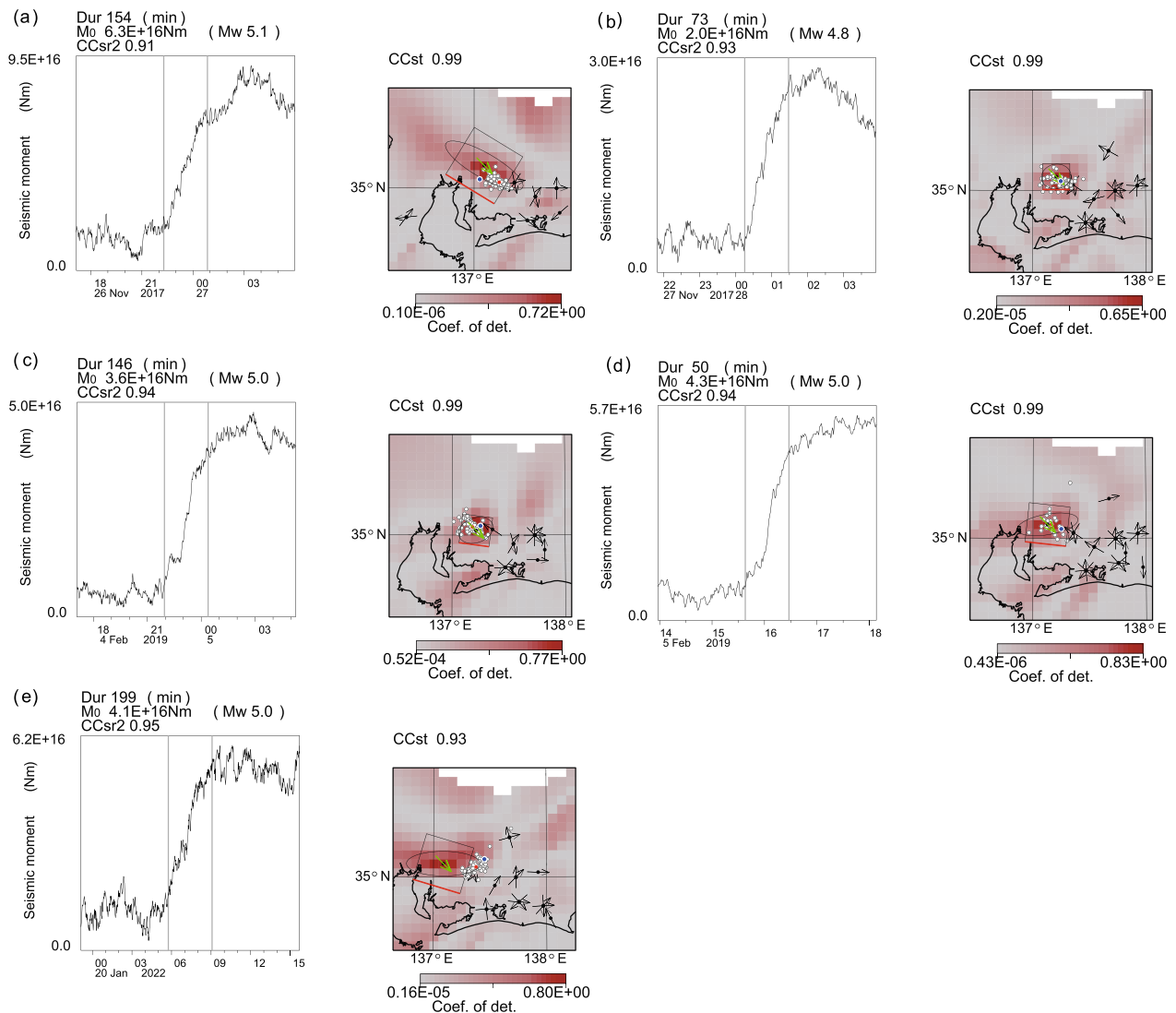


Fig. 5 Detected strain steps in the stacked strain from 2016 to 2022. **a–e** show the strain steps which indicated spatiotemporal correlations with tectonic tremor activities. Stacked strain changes are shown on the left side of each panel, and their r^2 distributions are shown on the right. Dur, M_0 , CC_{sr2} , and CC_{st} denote the estimated duration, the seismic moment, the correlation coefficient with a ramp function, and the correlation coefficient with the accumulated number of tectonic tremors of the strain step. The rectangle on each map shows a fault model used for the seismic moment estimation; the red line segment on the rectangle indicates the upper edge of the fault, and the green arrow indicates the slip direction. The blue dot indicates the fault center location assumed in the strain step detection described in “Detection of Strain Steps” section. Black circles with arrows indicate the locations of strainmeters used for the analysis, and the direction of each arrow indicates the strain-sensing direction. Open circles and the red dot denote the epicenters of tectonic tremors occurring during the strain step and their averaged location, respectively

little far from the assumed source location. The time window used for CC_{st} is five times of the estimated duration, with double time length before and after the duration of the strain step. CC_{st} of strain steps with concentrated r^2 distributions (Additional file 4: Fig. S4b,c,e) were more than 0.98. This indicates that such strain steps have a strong relationship with tremor activities.

In addition to time domain correlation, spatial correlation was considered using the Gaussian distribution fitted

to the r^2 distribution. We selected strain steps for which the averaged tremor epicenter (the red dot in Fig. 5) was within the ellipsoid fitted to r^2 distribution. Only five strain steps were found with this criterion from 2016 to 2022. They are shown in Fig. 5 and Table 2. Their durations were about 1–3 h. The strain steps in Fig. 5 were probably caused by plate boundary slip events because of the synchronous activation with tectonic tremors and the coincidence of source locations. Whereas the strain

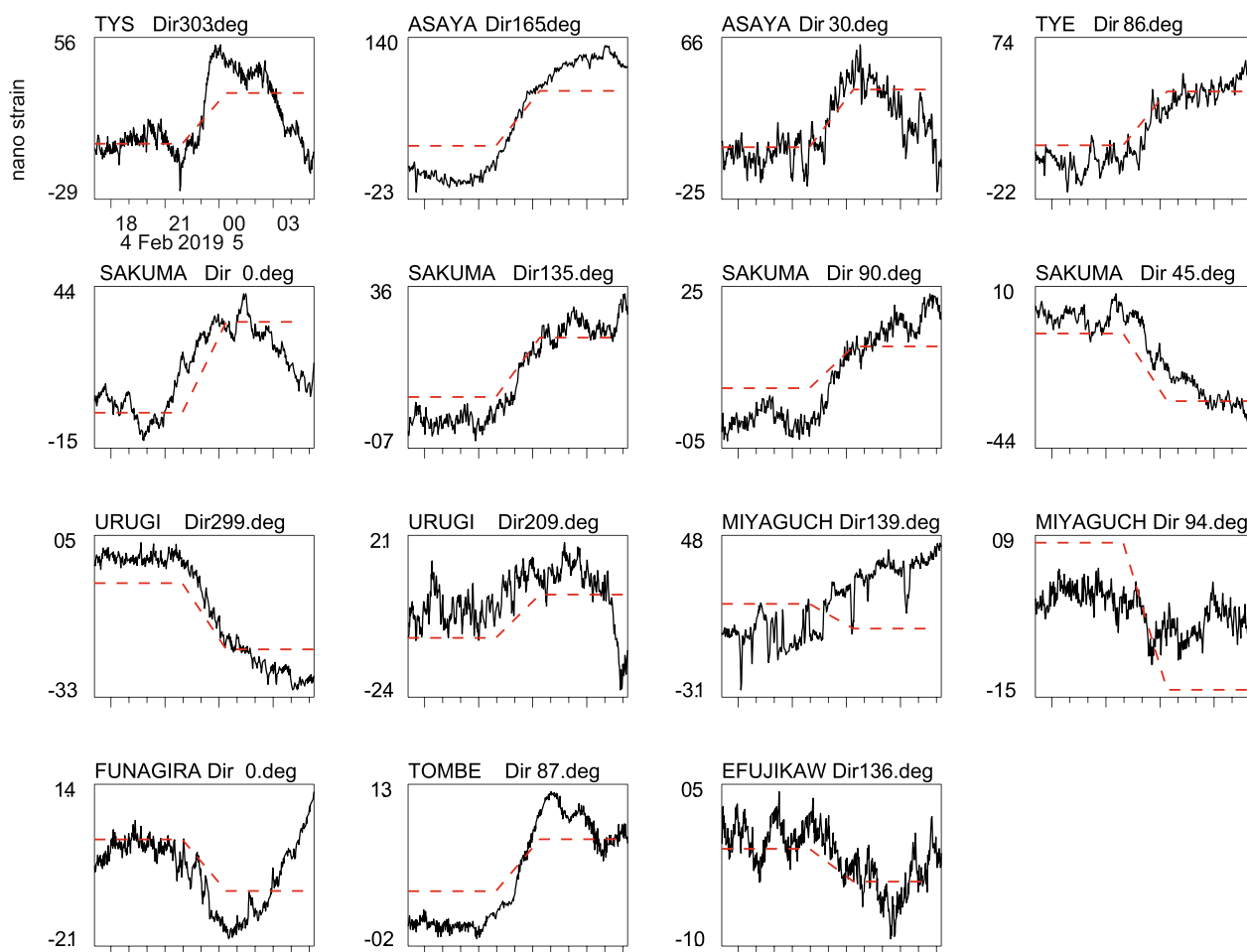


Fig. 6 Strain change of each sensor during the strain steps on 4 February, 2019 (Fig. 5c). The broken red line indicates the calculated strain change for the parameters shown in Table 2. Dir denotes the sensor orientation measured clockwise from the north

steps of Additional file 4: Fig S4e,f showed high values of CC_{st} , their high r^2 area did not share tremor-active region. There were 11 strain steps with $CC_{st} > 0.9$ from 2016 to 2022 including those shown in Additional file 4: Fig. S4. All of them occurred during S-SSEs. It might be possible that the strain steps in Additional file 4: Fig S4e,f were caused by plate boundary slip events. However, their reliability is lower than those in Table 2. Strain changes of individual sensors for Fig. 5c are shown in Fig. 6. The strain step at each sensor is not so evident as in the stacked strain.

All the strain steps in Fig. 5 occurred during S-SSEs, and they were considered to be slip speed variations during S-SSEs. Slip speed fluctuations have been reported for larger slow slip events by GNSS observations (e.g. Ozawa et al. 2005; Rousset et al. 2019; Yousofi et al. 2023). However, it has been difficult to detect slip speed fluctuations during slow earthquakes of M 6 class. Frank et al. (2018) showed that a large slow slip event (M_w 7.5) in

Mexico was a cluster of short-duration slow transients based on LFE activity analysis. Our observations showed the relationship between tremor activities and the slow plate boundary slip events directly for smaller events.

Discussion

It is apparent that detectable strain steps of 1–3 h duration occur infrequently. We thus infer that some special conditions must be met for a slip speed increase of 1–3 h duration to occur. The background S-SSE in February 2019 continues from February 3 to February 10 in the Tokai region (Japan Meteorological Agency 2019). Source migration and slip speed changes were observed in the S-SSE. Japan Meteorological Agency (2019) identified three stages in the event. They looked like successive occurrences of three S-SSEs. Strain steps in 5c,d occurred in the first stage. Such event groups are relatively rare, although a similar sequence of S-SSEs was observed in November 2017 (Japan Meteorological

Agency 2018) in the area covered by the stations listed in Table 1. In the case of the S-SSE in November 2017, two strain steps shown in Fig. 5 were observed. The strain step on 20 January 2022 (Fig. 5e) occurred during an S-SSE from 14 January to 2 February (Japan Meteorological Agency 2022). Source migration was also observed for this event (Japan Meteorological Agency 2022). The successive occurrence with source migration of S-SSEs may be related to the conditions necessary to provoke a temporary slip speed increase of about 1–3 h duration.

Tectonic tremor and VLFE activities become high during an S-SSE, and the synchronous activation of tremors and VLFEs has been observed (Ito et al. 2007). The strain steps detected in this study can be recognized as a phenomenon similar to tremor and VLFEs, which are recognized as parts of S-SSE activity. The strain steps of 1–3 h duration were observed simultaneously with tectonic tremor activation, and the detected slip speed change of 1–3 h duration, tectonic tremors, and S-SSE shared the same source locations. Therefore, tectonic tremors, VLFEs, this slip speed change of 1–3 h duration, and S-SSE are part of the same group of phenomena. The similarity between Fig 2c (detrended stacked strain) and Fig 2d (detrended accumulated number of tremors) indicates that more synchronous activations of tectonic tremors with plate boundary slip events of one to several

hours would have occurred than those shown in Fig. 5 and Table 2. However, step-like activation of tectonic tremors does not always accompany the step-like variation of strain as seen in Fig. 2. For example, clear strain steps are not seen on 4 February in Fig. 2c while some activations of tremors are recognized in Fig. 2d. Therefore, although tectonic tremor and the slip speed change of 1–3 h duration may share the same source area, they are not different aspects of a single phenomenon.

Figure 7 shows the epicenters of the tectonic tremors during an S-SSE from 3 February to 6 February in 2019 (black circles) and those during strain steps shown in Fig. 5c,d and Table 2 (red circles). Because tectonic tremors activated synchronously with the plate boundary slip event of an S-SSE as seen in Fig. 2c,d, the hypocenters of tectonic tremors would be related to the slip area of the S-SSE. The tremor-active area moved during the S-SSE. The tremor hypocenters during the strain steps in Fig. 5c,d (red circles in Fig. 7) would be related to slip areas that caused the strain steps. The red circles in the figure occupy only a part of the tremor active area during the S-SSE. This indicates that the plate boundary slip area during the strain steps would have been smaller than the whole slip area of the S-SSE.

Whereas the detected strain step was part of an S-SSE, the differential seismic moment during the

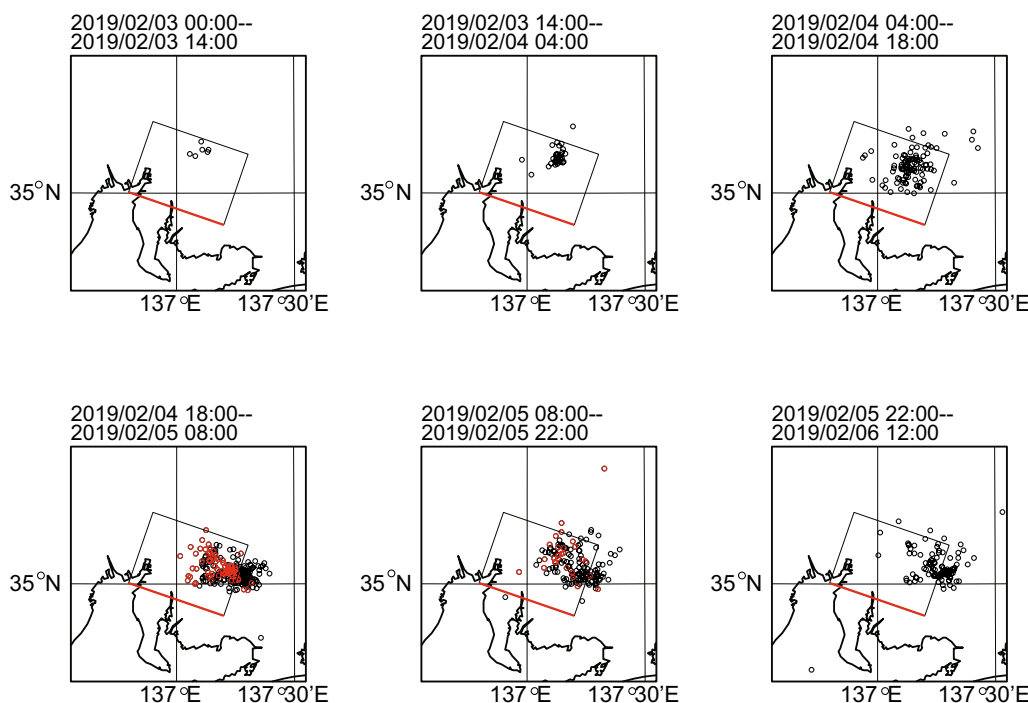


Fig. 7 Epicenter map of tectonic tremors estimated with the method of Imanishi et al. (2011) during an S-SSE from 3 February 2019 to 6 February 2019 (Japan Meteorological Agency 2019). The rectangle on each map shows a fault model of the S-SSE; the red line segment on the rectangle indicates the upper edge of the fault. The black circles denote tectonic tremor epicenters in the period shown at each panel, and the red circles tectonic tremor epicenters during the strain steps shown in Fig. 5c,d and Table 2

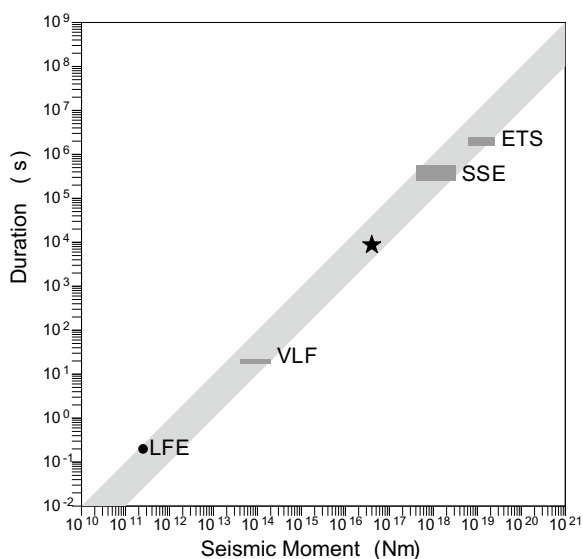


Fig. 8 The scaling law proposed by Ide et al. (2007). The star indicates the duration and seismic moment of the strain step shown in Fig. 5c

strain step can be calculated by detrending the stacked strain based on the strain change before the strain step. In Fig. 5 and Table 2, the differential seismic moment is shown. The moment magnitudes of the detected strain steps were estimated to be about M_w 5. The scaling law of Ide et al. (2007) for slow earthquakes is shown in Fig. 8 together with the duration and seismic moment of the event in Fig. 5c. The detected strain step is consistent with the scaling law of slow earthquakes. If the source area is assumed to be about 15 km × 15 km based on the tremor distribution (Fig. 7), the slip distance would be about 6 mm for an assumed rigidity of 30 GPa, which is of the same order as the slip events of other SSEs (Ide et al. 2007).

Conclusions

We researched strain steps with durations of about 1 h in the data of borehole and laser strainmeters. Some strain steps of 1–3 h durations simultaneously occurred with the activation of tectonic tremors, and it was estimated that they shared the same source locations with the tremors. They occurred during short-term slow slip events (S-SSEs), and were considered to be temporary slip speed increases during S-SSEs. Five strain steps were identified from 2016 to 2022. Two of them were during the successive occurrences with source migration of S-SSEs in 2017, two of them were during the successive occurrences of S-SSEs in 2019, and one of them was during source migration of S-SSEs in 2022. Successive occurrences with source migration of S-SSEs would be related to detectable slip speed changes of about 1 h. Detrended strain changes of those strain steps correspond to moment magnitudes

around 5.0, which is consistent with the scaling law for slow earthquakes proposed by Ide et al. (2007).

Abbreviations

- AIST: Advanced Industrial Science and Technology
- CC_{sr}: Correlation coefficient between stacked strain data and a ramp function
- CC_{sr2}: Correlation coefficient between stacked strain data and a ramp function using the data of CC_{ir} > 0.5
- CC_{ir}: Correlation coefficient between strain at an individual sensor and a ramp function
- CC_{st}: Correlation coefficient between the stacked strain and the accumulated number of tectonic tremors
- ERI: Earthquake Research Institute, The University of Tokyo
- JMA: Japan Meteorological Agency
- MRI: Meteorological Research Institute, JMA
- r²: Coefficient of determination
- SSE: Slow slip event
- S-SSE: Short-term slow slip event

Supplementary Information

The online version contains supplementary material available at <https://doi.org/10.1186/s40623-024-01983-z>.

Additional file 1: Figure S1. Station map with station codes. The blue triangles and rectangles show the borehole and laser strainmeter locations, respectively. Epicenters of the tectonic tremors from 2016 to 2022 estimated by the method of Imanishi et al. (2011) (red circles) and S-SSE source areas from 2021 to 2022 (e.g. Japan Meteorological Agency, 2021) (black rectangles) are also shown. The black dots show the assumed fault center locations used in the stacking method.

Additional file 2: Figure S2. Strain change at each sensor from 21 Jan. 2019 to 19 Feb. 2019.

Additional file 3: Figure S3. Stacked strain data and detection of strain steps. Every two pages show various graphs for assumed source locations shown in Fig. 1. (a) Stacked strain made from the strain data shown in Fig. S2. The assumed source location is shown at the top of the graph. Strain steps were searched for in the interval from 31 Jan. to 9 Feb. 2019 in this stacked strain time series. (b) Time series of correlation coefficients between stacked strain shown in (a) with a ramp function of 1 h rise time. (c) The same as (b) for 2 h rise time. (d) The same as (b) for 4 h rise time. (e) Detrended stacked strain of a 10-day interval. (f) Detrended accumulated number of tectonic tremors. The gray filled area in (e) and (f) indicates the interval with a high correlation between stacked strain and the ramp function of 1 or 2 h rise time (CC_{sr} > 0.88).

Additional file 4: Figure S4. Estimation of various parameters of strain steps with CC_{sr} > 0.88. Five or six panels are shown for each strain step. Upper left, time series of stacked strain. The vertical gray lines show the duration of the strain step. Upper center, relationship between CC_{sr2} and the assumed rise time of the ramp function. The horizontal line indicates

$$\text{the value of } \frac{1}{2} \log \frac{1+r}{1-r} = \frac{1}{2} \log \frac{1+r_p}{1-r_p} - \sqrt{\frac{1}{n-3}}, \text{ where } r$$

correlation coefficient, r_p peak value of r , and n number of data. The line was drawn to indicate r_p —(standard deviation of r). Upper right,

distribution of r^2 , where r^2 is a coefficient of determination between calculated and observed strains for the assumed source location. The ellipsoid on the map indicates a Gaussian distribution fitted to r^2 distribution. The rectangle on each map shows a fault model assumed in the strain step detection; the red line segment on the rectangle indicates the upper edge of the fault, and the green arrow indicates the slip direction. Black circles with arrows indicate the locations of strainmeters used for the analysis, and the direction of each arrow indicates the strain-sensing direction. Open circles denote the epicenters of tectonic tremors occurring during the strain step. The red dot is the average location of the plotted tremors. Lower left, relationship between calculated

and observed strains at an assumed source location with the highest r^2 in the upper right map. The line denotes the result of the regression analysis. Lower center, accumulated number of tectonic tremors during the time interval shown in the upper left panel. Lower right, time series of stacked strain for the source location based on the r^2 distribution. Fault length and width were assumed to be the average of the short and long diameters of the ellipsoid in the map of the upper right panel.

Acknowledgements

We are grateful to anonymous reviewers for their kind and informative comments. We used strain data obtained by Japan Meteorological Agency and National Institute of Advanced Industrial Science and Technology (AIST), tectonic tremor hypocenters estimated by AIST.

Author contributions

AK analyzed strain data and contributed to manuscript preparation. KM contributed to data analysis with the stacking method, and contributed to laser strainmeter observation at Funagira. TT contributed to data preparation of borehole strainmeters. SI contributed to data analysis of tectonic tremors. MT contributed to observation of Funagira laser strainmeter and the correction method for environmental data. TI contributed to the observation of Inuyama laser strainmeter. AT improved stabilization of the laser at Funagira. AA provided laser systems for Funagira and Inuyama strainmeters. All authors read and approved the final manuscript.

Funding

Japan Meteorological Agency and National Institute of Advanced Industrial Science and Technology installed and maintained their borehole strainmeters. Earthquake Research Institute of the University of Tokyo and Nagoya University installed and maintained the Inuyama laser strainmeter. Meteorological Research Institute and Earthquake Research Institute installed and maintained the Funagira laser strainmeter. The laser strainmeters used in this study were improved with the support of JSPS KAKENHI Grant Number JP17H06207.

Availability of data and materials

Strain data obtained by Japan Meteorological Agency analyzed during the current study are available at Crust Deformation Database repository (<https://nipe.sci.hokudai.ac.jp/db/login.php>). Parts of strain data obtained by National Institute of Advanced Industrial Science and Technology (AIST), those of the laser strainmeters, and tremor hypocenters by AIST shown in this article are accessible at <https://doi.org/10.5281/zenodo.7664373> (Katsumata 2023). S-SSe source parameters estimated by Japan Meteorological Agency are accessible from the links at <https://www.jma.go.jp/jma/press/hantei.html>. Other data are currently not publicly accessible. However, they could be available from each organization upon reasonable request.

Declarations

Competing interests

The authors declare that they have no competing interests.

Author details

¹Faculty of Sustainable Design, University of Toyama, Toyama 930-8555, Japan. ²Japan Meteorological Agency, Tokyo, Japan. ³Meteorological Research Institute, Japan Meteorological Agency, Tsukuba, Japan. ⁴National Institute of Advanced Industrial Science and Technology, Tsukuba, Japan. ⁵Meteorological Research Institute, Japan Meteorological Agency, Tsukuba, Japan. ⁶Nagoya University, Nagoya, Japan. ⁷Earthquake Research Institute, The University of Tokyo, Tokyo, Japan. ⁸Earthquake Research Institute, The University of Tokyo, Tokyo, Japan.

Received: 29 September 2023 Accepted: 16 February 2024

Published online: 18 March 2024

References

- Aiken C, Obara K (2021) Data-driven clustering reveals more than 900 small magnitude slow earthquakes and their characteristics. *Geophys Res Lett* 48:e2020GL091764. <https://doi.org/10.1029/2020GL091764>
- Araya A, Kunugi T, Fukao Y, Yamada I, Suda N, Maruyama S, Mio N, Moriwaki S (2002) Iodine-stabilized Nd:YAG laser applied to a long-baseline interferometer for wideband earth strain observations. *Rev Sci Instrum* 73:2434–2439. <https://doi.org/10.1063/1.1477606>
- Bletery Q, Thomas AM, Hawthorne JC, Skarbek RM, Rempel AW, Krogstad RD (2017) Characteristics of secondary slip fronts associated with slow earthquakes in Cascadia. *Earth Planet Sc Lett* 463:212–220. <https://doi.org/10.1016/j.epsl.2017.01.046>
- Cruz-Atienza VM, Tago J, Villafuerte C, Wei M, Garza-Girón R, Dominguez LA, Kostoglodov V, Nishimura T, Franco SI, Real J, Santoyo MA, Ito Y, Kazachkina E (2021) Short-term interaction between silent and devastating earthquakes in Mexico. *Nat Commun* 12:2171. <https://doi.org/10.1038/s41467-021-22326-6>
- Dragert H, Wang K, James TS (2001) A silent slip event on the deeper Cascadia subduction interface. *Science* 292:1525–1528. <https://doi.org/10.1126/science.1060152>
- Frank WB, Rousset B, Lasserre C, Campillo M (2018) Revealing the cluster of slow transients behind a large slow slip event. *Sci Adv* 4:eaat0661. <https://doi.org/10.1126/sciadv.aat0661>
- Fukao Y, Kubota T, Sugioka H, Ito A, Toneyawa T, Shiobara H, Yamashita M, Saito T (2021) Detection of “rapid” aseismic slip at the Izu-Bonin trench. *J Geophys Res-Sol Ea* 126:e2021JB022132. <https://doi.org/10.1029/2021JB022132>
- Ghosh A, Huesca-Pérez E, Brodsky E, Ito Y (2015) Very low frequency earthquakes in Cascadia migrate with tremor. *Geophys Res Lett* 42:3228–3232. <https://doi.org/10.1002/2015GL063286>
- Hawthorne JC, Rubin AM (2013) Short-time scale correlation between slow slip and tremor in Cascadia. *J Geophys Res-Sol Ea* 118:1316–1329. <https://doi.org/10.1002/jgrb.50103>
- Hirose H, Hirahara K, Kimata F, Fujii N, Miyazaki S (1999) A slow thrust slip event following the two 1996 Hyuganada earthquakes beneath the Bungo Channel, southwest Japan. *Geophys Res Lett* 26:3237–3240. <https://doi.org/10.1029/1999GL010999>
- Hirose H, Obara K (2005) Repeating short- and long-term slow slip events with deep tremor activity around the Bungo Channel region, southwest Japan. *Earth Planets Space* 57:961–972. <https://doi.org/10.1186/BF03351875>
- Hirose F, Nakajima J, Hasegawa A (2008) Three-dimensional seismic velocity structure and configuration of the Philippine Sea slab in southwestern Japan estimated by double-difference tomography. *J Geophys Res-Sol Ea* 113:B09315. <https://doi.org/10.1029/2007JB005274>
- Ide S, Beroza GC, Shelly DR, Uchide T (2007) A scaling law for slow earthquakes. *Nature* 447:76–79. <https://doi.org/10.1038/nature05780>
- Ide S, Beroza GC (2023) Slow earthquake scaling reconsidered as a boundary between distinct modes of rupture propagation. *Earth Atmos Pl Sc* 120:e2222102120. <https://doi.org/10.1073/pnas.2222102120>
- Imanishi K, Takeda N, Kuwahara Y, Koizumi N (2011) Enhanced detection capability of non-volcanic tremor using a 3-level vertical seismic array network, VA-net, in southwest Japan. *Geophys Res Lett* 38:L20305. <https://doi.org/10.1029/2011GL049071>
- Ishii H, Yamauchi T, Kusumoto F (1997) Development of high sensitivity borehole strain meters and application for rock mechanics and earthquake prediction study. *Rock Stress*. Balkema, Netherlands, pp 253–258
- Ishii H, Chen G, Ohnishi Y (1997) Estimation of far-field stresses from borehole strainmeter observations. *Rock Stress*. Balkema, Netherlands, pp 259–264
- Ito Y, Obara K, Shiomi K, Sekine S, Hirose H (2007) Slow earthquakes coincident with episodic tremors and slow slip events. *Science* 315:503–506. <https://doi.org/10.1126/science.1134454>
- Japan Meteorological Agency (2016) Report of Earthquake Assessment Committee for Areas under Intensified Measures against Earthquake Disaster 25 Jan. 2016. <https://www.data.jma.go.jp/svd/eqev/data/gaikyo/hantei20160125/mate02.pdf>. Accessed 29 Jun 2020 (In Japanese)

- Japan Meteorological Agency (2018) Crustal activity around the Nankai trough (November 2017 - April 2018). Rep Coord Comm Earthq Pred 100:219–239
- Japan Meteorological Agency (2019) Crustal activity around the Nankai trough (November 2018 - April 2019). Rep Coord Comm Earthq Pred 102:230–263
- Japan Meteorological Agency (2021) Nankai Trough earthquake information 5 Feb. 2021. https://www.jma.go.jp/jma/press/2102/05c/mate01_1.pdf. Accessed 25 Apr 2023 (In Japanese)
- Japan Meteorological Agency (2022) Crustal activity around the Nankai trough (November 2021 - April 2022). Rep Coord Comm Earthq Pred 108:359–415
- Kamigaichi O, Naito H, Yamamoto T, Yoshikawa S, Kokubo K, Miyaoka K (1999) Analysis on response character of JMA Ishii-type strainmeters. In: Prog Abstr Seismol Soc Japan 1999 Fall Meeting B72.
- Katsumata A, Kamaya N (2003) Low-frequency continuous tremor around the Moho discontinuity away from volcanoes in the southwest Japan. *Geophys Res Lett* 30:1020. <https://doi.org/10.1029/2002GL015981>
- Katsumata A, Yamamoto T, Kobayashi A, Hamada N, Yoshikawa S (2010) Evaluation of detection level of crustal deformation observation in the time domain through power spectrum analysis—investigation of a long-baseline laser extensometer. *J Geod Soc Japan* 56:107–116. <https://doi.org/10.11366/sokuchi.56.107>
- Katsumata A (2023). Strain data used to analyze slow slip events of one-hour duration. <https://doi.org/10.5281/zenodo.7664373>
- Kobayashi A, Yoshida A (2004) Recurrence of the Tokai slow slip inferred from the tide gauge data at Maisaka. *J Geod Soc Japan* 50:209–212
- Kobayashi A, Yamamoto T, Nakamura K, Kimura K (2006) Short-term slow slip events detected by the strainmeters in Tokai region in the period from 1984 to 2005. *J Seismol Soc* 59:19–27
- Kostoglodov V, Singh SK, Santiago JA, Franco SI, Larson KM, Lowry AR, Bilham R (2003) A large silent earthquake in the Guerrero seismic gap. *Mexico Geophys Res Lett* 30:1807. <https://doi.org/10.1029/2003GL017219>
- Miller MM, Melbourne T, Johnson DJ, Sumner WQ (2002) Periodic slow earthquakes from the Cascadia subduction zone. *Science* 295:2423. <https://doi.org/10.1126/science.1071193>
- Miyaoka K, Yokota T (2012) Development of stacking method for the detection of crustal deformation -application to the early detection of slow slip phenomena on the plate boundary in the Tokai region using strain data. *J Seismol Soc Japan* 65:205–218
- Nishimura T (2014) Short-term slow slip events along the Ryukyu Trench, southwestern Japan, observed by continuous GNSS. *Prog Earth Planet Sci* 1:22. <https://doi.org/10.1186/s40645-014-0022-5>
- Obara K (2002) Nonvolcanic deep tremor associated with subduction in southwest Japan. *Science* 296:1679–1681. <https://doi.org/10.1126/science.1070378>
- Obara K, Hirose H, Yamamizu F, Kasahara K (2004) Episodic slow slip events accompanied by non-volcanic tremors in southwest Japan subduction zone. *Geophys Res Lett* 31:L23602. <https://doi.org/10.1029/2004GL020848>
- Obara K, Ito Y (2005) Very low frequency earthquakes excited by the 2004 off the Kii peninsula earthquakes: a dynamic deformation process in the large accretionary prism. *Earth Planets Space* 57:321–326. <https://doi.org/10.1186/BF03352570>
- Okada Y (1992) Internal deformation due to shear and tensile faults in a half-space. *B Seismol Soc Am* 82:1018–1040. <https://doi.org/10.1785/BSSAO820021018>
- Okada Y, Nishimura T, Tabei T, Matsushima T, Hirose H (2022) Development of a detection method for short-term slow slip events using GNSS data and its application to the Nankai subduction zone. *Earth Planets Space* 74:18. <https://doi.org/10.1186/s40623-022-01576-8>
- Ozawa S, Murakami M, Kaidzu M, Hatanaka Y (2005) Transient crustal deformation in Tokai region, central Japan, until May 2004. *Earth Planets Space* 57:909–915. <https://doi.org/10.1186/BF03351870>
- Ozawa S, Tobita M, Yari H (2016) A possible restart of an interplate slow slip adjacent to the Tokai seismic gap in Japan. *Earth Planets Space* 68:54. <https://doi.org/10.1186/s40623-016-0430-4>
- Rogers G, Dragert H (2003) Episodic tremor and slip on the Cascadia subduction zone: the chatter of silent slip. *Science* 300:1942–1943. <https://doi.org/10.1126/science.1084783>
- Rousset B, Fu Y, Bartlow N, Bürgmann R (2019) Weeks-long and years-long slow slip and tectonic tremor episodes on the south central Alaska megathrust. *J Geophys Res-Sol Ea* 124:13392–13403. <https://doi.org/10.1029/2019JB018724>
- Seno T, Stein S, Gripp AE (1993) A model for the motion of the Philippine Sea Plate consistent with NUVEL-1 and geological data. *J Geophys Res-Sol Ea* 98:17941–17948. <https://doi.org/10.1029/93JB00782>
- Seshimo Y, Yoshioka S (2022) Spatiotemporal slip distributions associated with the 2018–2019 Bungo Channel long-term slow slip event inverted from GNSS data. *Sci Rep-UK* 12:343. <https://doi.org/10.1038/s41598-021-03982-6>
- Sugiyama T, Fujikoshi Y, Sugiura N, Kunitomo N (eds) (2007) Dictionary of statistical data science. Asakura shoten, Tokyo
- Tamura Y, Sato T, Ooe M, Ishiguro M (1991) A procedure for tidal analysis with a Bayesian information criterion. *Geophys J Int* 104:507–516. <https://doi.org/10.1111/j.1365-246X.1991.tb05697.x>
- Tsuyuki T, Hasegawa H, Chikasawa S, Kimura H, Tanada R, Numano A (2017) Improvements of crustal movement monitoring methods in the new earthquake phenomena observation system (EPOS). *Quat J Seismol* 81:5
- Wallace LM, Beavan J (2010) Diverse slow slip behavior at the Hikurangi subduction margin, New Zealand. *J Geophys Res-Sol Ea* 115:B12402. <https://doi.org/10.1029/2010JB007717>
- Yousfi ZE, Radiguet M, Rousset B, Husker A, Kazachkina E, Kostoglodov V (2023) Intermittence of transient slow slip in the Mexican subduction zone. *Earth Planet Sc Lett* 620:118340. <https://doi.org/10.1016/j.epsl.2023.118340>

Publisher's Note

Springer Nature remains neutral with regard to jurisdictional claims in published maps and institutional affiliations.